Chemical Science

ROYAL SOCIETY OF CHEMISTRY

EDGE ARTICLE

View Article Online
View Journal | View Issue



Cite this: *Chem. Sci.*, 2025, **16**, 20544

All publication charges for this article have been paid for by the Royal Society of Chemistry



# Constructing a visible-light-excited Z-scheme heterojunction by engineering the directional N–C/Cu insertion layer: overcoming work function mismatches

Hao Gao,†[a] Xiaoxiao He,†[b] Jinbu Li,†[a] Qiang Zhu,[a] Chengyu Qin,[a] Liming Sun,*[a] Shuting Zhi,[a] Lei Yang,[c] Wenwen Zhan,*[a] Jianwei Zhao[c] and Xiguang Han *[a]

The construction of S-scheme heterojunctions is constrained by stringent work function ($\Phi$) matching between oxidation and reduction photocatalysts, which limits material selection. Here, we present an innovative interfacial engineering strategy to overcome $\Phi$-mismatched barriers by introducing a nitrogen-doped carbon (N–C) mediator and Cu nanoparticles at the $WO_3/Cu_2O$ interface. Through a "post-deposition and pyrolysis" approach, we fabricated a tightly integrated Z-scheme $WO_3$/N–C/Cu/$Cu_2O$ heterojunction, where the N–C layer and metallic Cu synergistically redirect photogenerated carrier recombination, preserving the high redox potentials of $WO_3$ (VB: +2.62 V) and $Cu_2O$ (CB: −1.41 V). Femtosecond transient absorption spectroscopy and electron paramagnetic resonance data revealed that interfacial electrons from $WO_3$ transferred to N–C and recombined with holes originating from $Cu_2O$ on Cu *via* the directional N–C/Cu insertion layer. The optimized heterojunction exhibits exceptional photocatalytic performance under blue light (450 nm), achieving a 99% yield in homo-coupling of terminal alkynes to 1,3-conjugated diynes and a hydrogen evolution rate 300-fold higher than that of conventional $WO_3/Cu_2O$. This work provides a universal paradigm for designing Z-scheme systems with mismatched components, unlocking new possibilities for solar energy conversion and organic synthesis.

Received 18th July 2025
Accepted 27th September 2025

DOI: 10.1039/d5sc05362e

rsc.li/chemical-science

## Introduction

Photocatalytic systems, which harness solar energy to drive redox reactions, hold immense potential for sustainable energy conversion and organic synthesis.[1–5] However, their efficiency is fundamentally limited by rapid charge recombination and inadequate redox potentials.[6,7] Heterojunction photocatalysts, particularly step-scheme (S-scheme) systems, have emerged as a promising strategy to enhance charge separation while preserving strong redox capabilities (Scheme 1).[8–17] In S-scheme heterojunctions, the band bending, a built-in electric field and coulombic attraction at the interface between oxidation photocatalysts (OP) and reduction photocatalysts (RP) promote selective recombination of low-energy carriers, retaining high-energy electrons and holes for surface reactions.[18–25] However, the construction of S-scheme heterojunctions for photocatalytic applications encounters two primary challenges. Firstly, optimizing the bandgaps is critical. To facilitate the step-scheme migration of photogenerated carriers in S-scheme heterojunctions, both components must be simultaneously photoexcited.[26,27] However, selecting narrow-bandgap semiconductors to ensure a visible light response may compromise the overall redox capability of the S-scheme heterojunction photocatalytic system. Secondly, work function ($\Phi$) matching between components is essential.[28–30] The formation of an S-scheme heterojunction mandates that the work function of the RP is lower than that of the OP ($\Phi_{RP} < \Phi_{OP}$). These challenges severely limit material selection and often exclude semiconductors with superior light absorption or catalytic activity.

$WO_3$ and $Cu_2O$, as visible-light-responsive OP and RP candidates, exemplify this dilemma and have been excluded as S-scheme heterojunction candidates.[31–33] $WO_3$ possesses a highly positive valence band ideal for oxidation,[34–40] while $Cu_2O$ offers a negative conduction band suitable for reduction.[41–44] However, their intrinsic work function mismatch ($\Phi_{WO_3} < \Phi_{Cu_2O}$) leads to the formation of undesired II-type heterojunctions other than S-scheme heterojunctions, where electrons accumulate in the CB of $WO_3$ and holes in the VB of $Cu_2O$, drastically diminishing their redox potentials. Previous

[a]Jiangsu Key Laboratory of Green Synthetic Chemistry for Functional Materials, Department of Chemistry, School of Chemistry & Materials Science, Jiangsu Normal University, Xuzhou, 221116, P. R. China
[b]State Key Laboratory of Precision Spectroscopy, East China Normal University, Shanghai, 200241, P. R. China
[c]Shenzhen HUASUAN Technology Co., Ltd, Shenzhen, 518055, P. R. China
† These authors contributed equally.

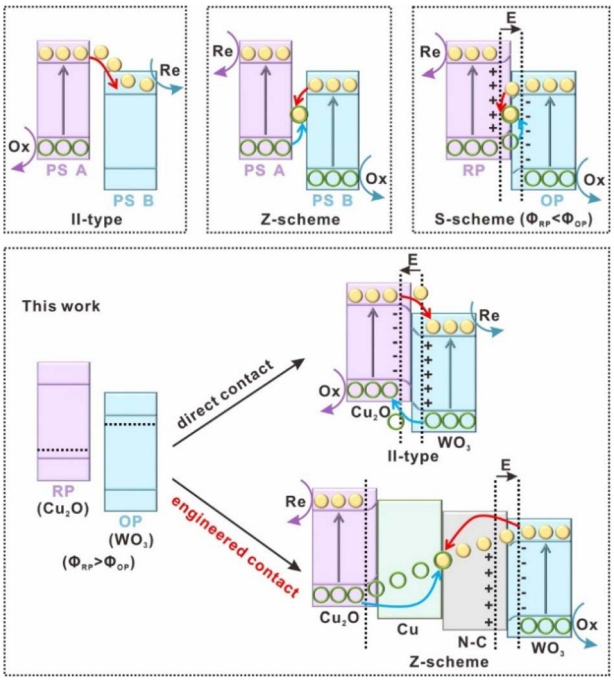


Scheme 1 The schematic diagram of the migration and separation pathways of photogenerated carriers in II-type, Z-scheme, and S-scheme heterojunctions, as well as the heterojunctions developed in this work.

attempts to address this challenge, such as doping or morphology tuning, have failed to reconcile interfacial energetics with efficient charge dynamics, leaving the core issue of $\Phi$-mismatch unresolved.

Herein, we propose an interfacial engineering strategy to override the work function limitation by introducing a nitrogen-doped carbon (N–C) mediator and metallic Cu nanoparticles at the $WO_3/Cu_2O$ interface. The N–C layer, with a low $\Phi$, creates a directional electron transfer pathway from N–C to $WO_3$, while Cu nanoparticles act as hole reservoirs for $Cu_2O$, collectively reshaping the built-in electric field to form a Z-scheme heterojunction. Through a "post-deposition and pyrolysis" synthetic approach, we constructed a tightly integrated $WO_3$/N–C/Cu/$Cu_2O$ heterojunction, where transient absorption and *in situ* electron paramagnetic resonance data confirm that photogenerated electrons from $WO_3$ transfer to N–C and recombine with holes from $Cu_2O$ on Cu nanoparticles *via* the N–C/Cu interface, preserving the high-energy carriers for redox reactions. The optimized system achieves a 99% yield in terminal alkyne homo-coupling and a hydrogen evolution rate 300-fold higher than that of conventional $WO_3/Cu_2O$ under the illumination of a blue light-emitting diode (LED). This work not only resolves the long-standing $\Phi$-mismatch challenge but also establishes a universal interfacial engineering paradigm for constructing Z-scheme systems from incompatible components. By decoupling material selection from intrinsic electronic constraints, our strategy opens new avenues for developing high-performance photocatalysts tailored for solar fuel production and organic transformations.

## Results and discussion

The synthesis procedure of mesoporous $WO_3$/N–C/Cu/$Cu_2O$ cuboctahedra *via* the "post-deposition and pyrolysis" method is schematically illustrated in Fig. 1a. First, well-defined HKUST-1 with a cuboctahedral structure was synthesized through a simple solvothermal reaction, utilizing copper nitrate trihydrate ($Cu(NO_3)_2 \cdot 3H_2O$) as the metal salt, 1,3,5-benzenetricarboxylic acid as the organic ligand, and benzimidazole as the modulator. For detailed experimental procedures, please refer to the SI. Then, the obtained HKUST-1 precursor and monoclinic $WO_3$ (the relevant preparation and characterization details are presented in the SI and Fig. S1) were uniformly immersed in methanol. Subsequently, the mixture was heated at 120 °C for 6 hours. During this treatment, the cuboctahedral $WO_3$/HKUST-1 precursor could be obtained. Afterward, a pyrolysis treatment was carried out at 300 °C in an Ar atmosphere, and $Cu^{2+}$ ions within the $WO_3$/HKUST-1 precursor were transformed into $Cu_2O$ and metallic Cu. Simultaneously, benzimidazole and 1,3,5-benzenetricarboxylic acid underwent *in situ* carbonization to form an external N–C layer. As a result, the $WO_3$/HKUST-1 precursor evolved into mesoporous cuboctahedral $WO_3$/N–C/Cu/$Cu_2O$.

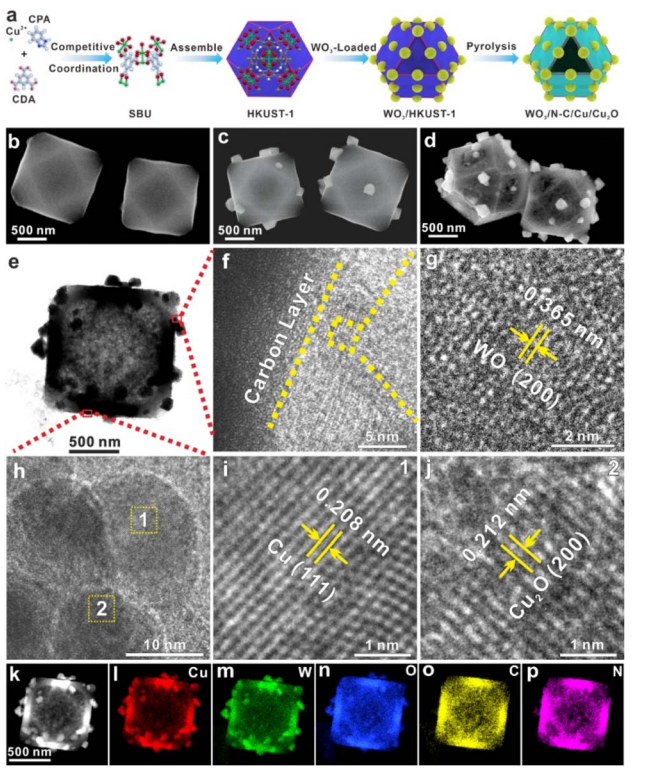


Fig. 1 (a) Schematic showing the synthetic process of $WO_3$/N–C/Cu/$Cu_2O$, FE-SEM images of (b) the cuboctahedral HKUST-1 precursor, (c) the cuboctahedral $WO_3$/HKUST-1 precursor, and (d) $WO_3$/N–C/Cu/$Cu_2O$, (e) TEM image of $WO_3$/N–C/Cu/$Cu_2O$, (f) the magnified TEM image of the marked area in (e), (g) the corresponding HRTEM of the marked area in (f), (h) the magnified TEM image of the marked area in (e), (i and j) the corresponding HRTEM images of areas 1 and 2 in (h), (k) STEM image of $WO_3$/N–C/Cu/$Cu_2O$, and (l–p) EDX elemental mapping of Cu, W, O, C and N elements.

The composite and structure of the products obtained at different stages were characterized by powder X-ray diffraction (XRD) and field-emission scanning electron microscopy (FE-SEM). The XRD pattern of the HKUST-1 precursor is shown in Fig. S2. The precursor exhibits sharp diffraction peaks in good agreement with the simulated pattern of HKUST-1 with high crystallinity.[45] The FE-SEM image (Fig. 1b) shows that the prepared HKUST-1 precursor possesses a cuboctahedral morphology characterized by high uniformity and a smooth surface. After the deposition of $WO_3$, the resulting products (Fig. 1c) maintain a uniform cuboctahedral structure with excellent monodispersity, and their surfaces are decorated with small particles. As revealed by XRD analysis (Fig. S3a), the diffraction peaks are well consistent with those of the monoclinic $WO_3$ phase (PDF no. 01-072-1465) and the simulated HKUST-1 pattern, thereby confirming the coexistence of $WO_3$ and HKUST-1 in the composite sample $WO_3$/HKUST-1. The simultaneous presence of Cu, W, O, C and N elements in $WO_3$/HKUST-1 was revealed by energy-dispersive X-ray spectroscopy (EDX) elemental mapping (Fig. S3b–h). After annealing treatment in an Ar atmosphere, the $WO_3$/HKUST-1 phase transformed into $WO_3$/N–C/Cu/$Cu_2O$. The XRD pattern shown in Fig. S4 demonstrates a good match between the diffraction peaks of the annealed product and monoclinic $WO_3$ (PDF no. 01-072-1465), cubic $Cu_2O$ (PDF no. 01-077-0199), and cubic Cu (PDF no. 00-004-0836). The Raman spectrum of $WO_3$/N–C/Cu/$Cu_2O$ (Fig. S5) shows a D-band peak at 1344 $cm^{-1}$ and a G-band peak at 1562 $cm^{-1}$, which are related to defective graphitic carbon. These results provide strong evidence for the successful phase transformation to $WO_3$/N–C/Cu/$Cu_2O$. The $WO_3$/N–C/Cu/$Cu_2O$ composite has maintained the cuboctahedral morphology of the $WO_3$/HKUST-1 precursor, but underwent a structural change from a solid to a hollow configuration, as depicted in Fig. 1d. The porosity of the obtained $WO_3$/N–C/Cu/$Cu_2O$ composite was characterized using nitrogen adsorption–desorption isotherms (Fig. S6). The Barrett–Joyner–Halenda (BJH) pore size distribution has been determined to be approximately 19 nm, and the Brunauer–Emmett–Teller (BET) surface area of $WO_3$/N–C/Cu/$Cu_2O$ has been measured to be around 61.6 $m^2\ g^{-1}$.

The structure and components of $WO_3$/N–C/Cu/$Cu_2O$ were comprehensively investigated using transmission electron microscopy (TEM). The TEM image (Fig. 1e) reveals that the synthesized $WO_3$/N–C/Cu/$Cu_2O$ exhibits a hollow cuboctahedral morphology, accompanied by dispersed small particles. The magnified TEM image (Fig. 1f) clearly reveals the presence of a well-defined heterojunction interface between the dispersed particles and the amorphous carbon layers. The HRTEM (high-resolution TEM) image of the marked yellow zone of the dispersed particle in Fig. 1f is depicted in Fig. 1g. The lattice spacing of 0.365 nm can be ascribed to the (200) plane of the monoclinic $WO_3$ phase, thereby indicating that the dispersed particle is a $WO_3$ particle. The magnified TEM image (Fig. 1h, red zone in Fig. 1e) indicates that the shell structure of the hollow cuboctahedra is assembled by nanoparticles. The HRTEM image of zone 1 in Fig. 1h (Fig. 1i) exhibits a lattice spacing of 0.208 nm, corresponding to the (111) plane of the cubic Cu phase. The HRTEM image of zone 2 in Fig. 1h (Fig. 1j) displays a lattice spacing of 0.212 nm, which can be attributed to the (200) plane of the cubic $Cu_2O$ phase. The presence of the Cu/$Cu_2O$ heterojunction interface can be confirmed by these findings. The high-angle annular dark-field scanning transmission electron microscope (HAADF-STEM) images in Fig. 1k further verify the existence of a hollow structure with small particles on the surfaces. The energy-dispersive X-ray spectroscopy (EDX) mapping (Fig. 1l–p) reveals a homogeneous distribution of Cu, W, O, C, and N elements within the cuboctahedral framework. The combination of XRD, HRTEM, and EDX analyses provides robust evidence for the successful synthesis of hollow cuboctahedra featuring a $WO_3$/N–C/Cu/$Cu_2O$ interface.

The synthesized $WO_3$/N–C/Cu/$Cu_2O$ heterojunctions were further analyzed using X-ray photoelectron spectroscopy (XPS) to determine the chemical states and static electron transfer between heterojunctions (Fig. S7 and 2a–d). To explore the electronic interactions among the components of the $WO_3$/N–C/Cu/$Cu_2O$ heterojunction, $WO_3$/$Cu_2O$ (details in the SI and Fig. S8), N–C/Cu/$Cu_2O$ (details in the SI and Fig. S9), $WO_3$, and $Cu_2O$ (details in the SI and Fig. S10) were employed as reference samples. As illustrated in Fig. 2a, the characteristic peaks located at 35.5 eV and 37.7 eV in the W 4f XPS spectrum of pristine $WO_3$ are attributed to the W $4f_{7/2}$ and W $4f_{5/2}$ of $W^{6+}$, respectively.[46] Compared with pristine $WO_3$, the W 4f peaks of the $WO_3$/N–C/Cu/$Cu_2O$ heterojunction have shifted to a lower energy region, indicating that $WO_3$ in this heterojunction is in an electron-acquiring state. In contrast, $WO_3$ in the $WO_3$/$Cu_2O$ heterojunction is in the opposite state since the W 4f peaks have shifted to a higher energy region relative to pristine $WO_3$. In Fig. 2b, the peaks at binding energies of 932.8 eV and 952.6 eV are assigned to Cu $2p_{3/2}$ and Cu $2p_{1/2}$ of $Cu^+/Cu^0$ in the N–C/Cu/$Cu_2O$ heterojunction, respectively. Meanwhile, the remaining

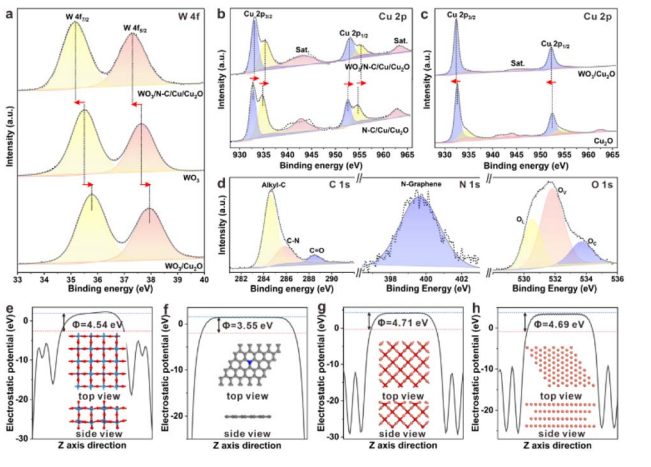


Fig. 2 (a) W 4f XPS of $WO_3$/N–C/Cu/$Cu_2O$, N–C/Cu/$Cu_2O$ and $WO_3$, (b) Cu 2p XPS of $WO_3$/N–C/Cu/$Cu_2O$ and N–C/Cu/$Cu_2O$, (c) Cu 2p XPS of $WO_3$/$Cu_2O$ and $Cu_2O$, and (d) C 1s, N 1s, and O 1s XPS of $WO_3$/N–C/Cu/$Cu_2O$. The electrostatic potentials and corresponding models of (e) $WO_3$, (f) N–C, (g) $Cu_2O$ and (h) Cu. The red, light blue, grey, blue, and orange spheres represent O, W, C, N, and Cu atoms, respectively. Blue and red dashed lines indicate the vacuum and Fermi energy levels.

peaks (934.8 eV and 954.7 eV) can be assigned to $Cu^{2+}$, which is due to the surface oxidation of $Cu^{+}$ ions and $Cu^{0}$. In comparison with N–C/Cu/$Cu_2O$, the Cu 2p peaks in the $WO_3$/N–C/Cu/$Cu_2O$ heterojunction shift towards a higher energy region. Combined with the previous analysis of the W 4f XPS spectra, this shift indicates the directed transfer of interfacial electrons to $WO_3$ from N–C/Cu/$Cu_2O$ during the formation of the $WO_3$/N–C/Cu/$Cu_2O$ heterojunctions. Meanwhile, Fig. 2c indicates that the characteristic peaks of $Cu^{+}$ in the $WO_3$/$Cu_2O$ heterojunction shift towards a lower binding energy, and no characteristic peaks of $Cu^{2+}$ are detected. This observation indicates that in the $WO_3$/$Cu_2O$ heterojunction, interfacial electrons transfer from $WO_3$ to $Cu_2O$, supported by the above analysis of the W 4f XPS spectra. Fig. 2d presents the XPS spectra of C 1s, N 1s, and O 1s in the $WO_3$/N–C/Cu/$Cu_2O$ heterojunction. In the C 1s XPS spectra, the peak at 284.8 eV corresponds to alkyl-C bonds, the peak at 286.1 eV is associated with $sp^2$-carbon containing nitrogen atoms (C–N bonds), and the peak at 288.7 eV is assigned to carbon atoms bonded to carbonyl groups (C═O). The N 1s peak at 399.6 eV can be attributed to graphene-N, further confirming N doping within the carbon layer. The high-resolution O 1s spectrum can be deconvoluted into three major peaks centered at 530.7 eV, 532.0 eV, and 533.6 eV, corresponding to lattice oxygen ($O_L$), oxygen-deficient regions ($O_V$), and dissociated and chemisorbed oxygen ($O_C$), respectively. The analysis of XPS spectra not only clarifies the chemical states and elemental compositions within the synthesized $WO_3$/N–C/Cu/$Cu_2O$ heterojunction but also indicates an interesting phenomenon, *i.e.*, the direction of interfacial electron migration is opposite in $WO_3$/N–C/Cu/$Cu_2O$ and $WO_3$/$Cu_2O$ heterojunctions.

To investigate the reason for the opposite direction of interfacial electron migration, we calculated the work functions ($\Phi$) of $WO_3$, the N–C layer, $Cu_2O$, and Cu, since the work function is a critical parameter for understanding interfacial charge transfer mechanisms.[47] As shown in Fig. 2e–h, the work functions of $WO_3$, the N–C layer, $Cu_2O$, and Cu have been calculated to be 4.54 eV, 3.55 eV, 4.71 eV, and 4.69 eV, respectively. The work function of $WO_3$ is lower than that of $Cu_2O$, which facilitates the migration of interfacial electrons from $WO_3$ to $Cu_2O$ when forming a $WO_3$/$Cu_2O$ heterojunction upon direct contact. Consequently, an internal electric field directed from $Cu_2O$ to $WO_3$ is established at the $WO_3$/$Cu_2O$ interface. In contrast, when $WO_3$ is in direct contact with the N–C layer, the lower work function of the N–C layer than $WO_3$ leads to electron transfer from the N–C layer to $WO_3$ at the interface, resulting in a built-in electric field oriented from the N–C layer toward $WO_3$. The differences in work functions among $WO_3$, the N–C layer, and $Cu_2O$ offer a reasonable explanation for the opposing directions of interfacial electron migration observed during the formation of the $WO_3$/N–C/Cu/$Cu_2O$ and $WO_3$/$Cu_2O$ heterojunctions. The distinct directions of electron migration at these interfaces result in oppositely oriented built-in electric fields, which underpin the II-type transfer mechanism of photogenerated carriers in the $WO_3$/$Cu_2O$ heterojunction and the Z-scheme transfer mechanism of photogenerated carriers in the $WO_3$/N–C/Cu/$Cu_2O$ heterojunction.

UV-vis diffuse reflectance spectra and valence band XPS spectra (VB-XPS) have been recorded to investigate the optical properties and the band positions of the catalysts. As shown in Fig. S11a, the optical absorption edges of pristine $WO_3$ and $Cu_2O$ fall within the visible light spectrum, thereby endowing the $WO_3$/N–C/Cu/$Cu_2O$ heterojunction with excellent light response properties in this region. The intrinsic band gap values ($E_g$) of pristine $WO_3$ and $Cu_2O$ are estimated to be 2.54 eV and 1.82 eV, respectively (Fig. S11b). The valence band potential ($E_{VB}$) can be evaluated using VB-XPS spectra. According to Fig. S11c, the $E_{VB}$ values of pristine $WO_3$ and $Cu_2O$ are measured to be 2.62 V and 0.41 V (*vs.* NHE), respectively. The conduction band potential ($E_{CB}$) can be calculated using the equation $E_g = E_{CB} - E_{VB}$.[57] Therefore, the $E_{CB}$ values for $WO_3$ and $Cu_2O$ are estimated to be 0.08 V and −1.41 V (*vs.* NHE), respectively.

Electron paramagnetic resonance (EPR) measurements have also been conducted to systematically study the mechanisms of charge separation and transfer in the $WO_3$/N–C/Cu/$Cu_2O$ heterojunction. Superoxide ($\cdot O_2^-$) and hydroxyl ($\cdot$OH) radicals can be trapped by 5,5-dimethyl-1-pyrroline N-oxide (DMPO), a well-established spin-trapping agent, and subsequently detected through EPR spectroscopy. As illustrated in Fig. 3a and

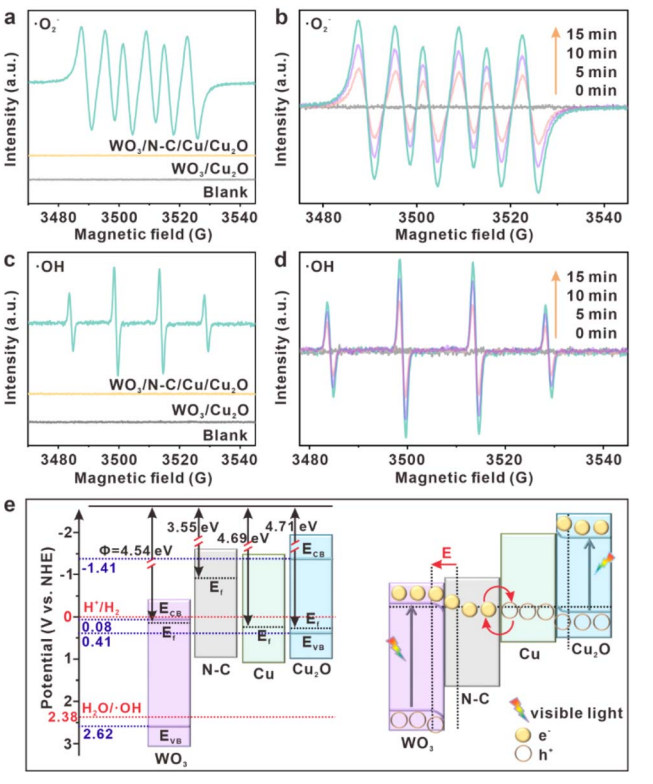


Fig. 3 EPR spectra of DMPO-·$O_2^-$ (a) in the presence of $WO_3$/N–C/Cu/$Cu_2O$ and $WO_3$/$Cu_2O$ heterojunctions upon irradiation with blue LEDs for 15 min and (b) in the presence of $WO_3$/N–C/Cu/$Cu_2O$ upon irradiation with blue LEDs for 0, 5, 10 and 15 min. EPR spectra of DMPO-·OH (c) in the presence of $WO_3$/N–C/Cu/$Cu_2O$ and $WO_3$/$Cu_2O$ heterojunctions upon irradiation with blue LEDs for 15 min and (d) in the presence of $WO_3$/N–C/Cu/$Cu_2O$ upon irradiation with blue LEDs for 0, 5, 10 and 15 min. (e) The Z-scheme charge transfer mechanism in $WO_3$/N–C/Cu/$Cu_2O$ under visible light irradiation.

c, no signal can be detected under dark conditions. Under 15 min of blue LED irradiation, the characteristic peaks of DMPO-·$O_2^-$ and DMPO-·OH have been detected in the $WO_3$/N–C/Cu/$Cu_2O$ heterojunction, while no such signals can be detected in the $WO_3$/$Cu_2O$ heterojunction. Based on the aforementioned information, it is evident that the CB position of $Cu_2O$ is more negative than the $O_2/\cdot O_2^-$ potential (−0.33 V *vs.* NHE), while the VB position of $WO_3$ is more positive than the $H_2O/\cdot OH$ potential (2.38 V *vs.* NHE). In contrast, the CB position of $WO_3$ is more positive than the $O_2/\cdot O_2^-$ potential, and the VB potential of $Cu_2O$ is more negative than the $H_2O/\cdot OH$ potential. Therefore, the simultaneous generation of $\cdot O_2^-$ and ·OH under light irradiation indicates that when the $WO_3$/N–C/Cu/$Cu_2O$ heterojunction as the catalyst participates in the reaction, the photogenerated electrons are ultimately enriched in the CB of $Cu_2O$, while the photogenerated holes are accumulated in the VB of $WO_3$. This provides strong evidence for the Z-scheme transfer mechanism in the $WO_3$/N–C/Cu/$Cu_2O$ heterojunction. Neither $\cdot O_2^-$ nor ·OH is produced in $WO_3$/$Cu_2O$ under light irradiation, consistent with the II-type charge transfer mechanism in the $WO_3$/$Cu_2O$ heterojunction. In addition, as exhibited in Fig. 3b and d, the peak intensities of $\cdot O_2^-$ and ·OH radicals in $WO_3$/N–C/Cu/$Cu_2O$ gradually increase with prolonged *in situ* irradiation time. This indicates that the Z-scheme structure facilitates efficient separation and transfer of photogenerated carriers, thereby promoting the generation of more active radical species. The above results from EPR and XPS confirm that inserting the N–C layer and Cu into the interfaces of the $WO_3$/$Cu_2O$ heterojunction enables the formation of a Z-scheme $WO_3$/N–C/Cu/$Cu_2O$ heterojunction.

The Z-scheme transfer mechanism of photogenerated carriers in the $WO_3$/N–C/Cu/$Cu_2O$ heterojunction under light illumination is further illustrated in Fig. 3e. When all the catalysts ($WO_3$, N–C layer, Cu, and $Cu_2O$) are in contact, three distinct interfaces are formed. Given that the N–C layer has a lower work function than $WO_3$, electrons spontaneously transfer from the N–C layer to $WO_3$ until the Fermi level at the interface reaches equilibrium. This electron redistribution at the $WO_3$/N–C interface results in band bending and a built-in internal electric field near the interface. Due to the similar work functions of Cu and $Cu_2O$, they can form an ohmic contact directly. Upon illumination, $WO_3$ and $Cu_2O$ become excited and generate electron–hole pairs. Under the influence of the internal electric field and band bending, the photogenerated electrons from the CB of $WO_3$ are driven towards the N–C layer. Due to the ohmic contact and the p-type characteristic of $Cu_2O$, the photogenerated holes from the VB of $Cu_2O$ transfer to Cu while simultaneously consuming photogenerated electrons on the N–C layer. Consequently, the oxidation-type photocatalyst of $WO_3$ forms hole-rich regions, whereas the reduction-type photocatalyst of $Cu_2O$ forms electron-rich regions. This process effectively enhances the transport of photogenerated charge carriers and maintains the high redox capability in the $WO_3$/N–C/Cu/$Cu_2O$ heterojunction.

The charge transfer dynamics of the Z-scheme $WO_3$/N–C/Cu/$Cu_2O$ heterojunction has been investigated by femtosecond transient absorption (fs-TA) spectroscopy. As shown in Fig. 4a,

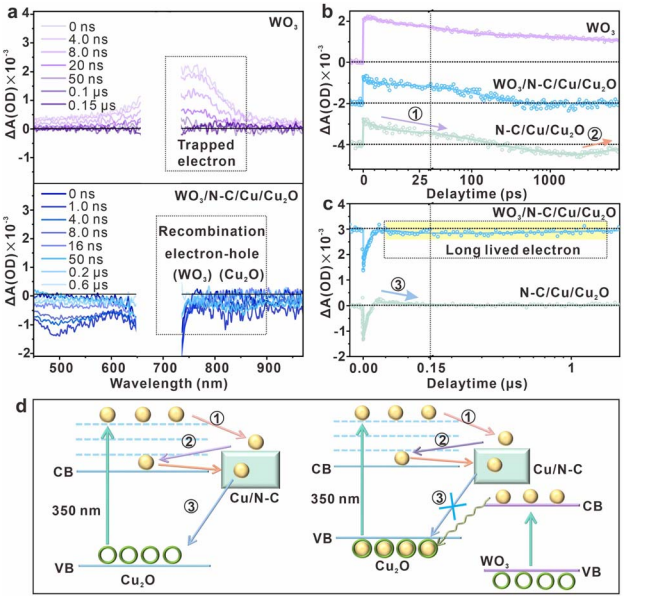


Fig. 4 (a) Transient absorption spectra of $WO_3$/N–C/Cu/$Cu_2O$ and $WO_3$. (b and c) Kinetics of $WO_3$/N–C/Cu/$Cu_2O$, N–C/Cu/$Cu_2O$ and $Cu_2O$ at 750 nm. (d) Schematic diagram of charge migration paths in N–C/Cu/$Cu_2O$ and $WO_3$/N–C/Cu/$Cu_2O$.

pristine $WO_3$ exhibits a pronounced excited-state absorption (ESA) signal ($\Delta A > 0$) at 750 nm. According to previous research reports,[58] this signal is attributed to defect-trapped electrons. Notably, after constructing the $WO_3$/N–C/Cu/$Cu_2O$ heterojunction, the ESA signal at 750 nm has completely vanished and is replaced by a ground-state bleaching (GSB, $\Delta A < 0$) signal. This signal inversion demonstrates that interfacial charge transfer efficiently quenches defect-trapped electrons in $WO_3$. Combined with the energy structure analysis (Fig. 3e), it is evident that the conduction band (CB) electrons of $WO_3$ preferentially recombine with the valence band (VB) holes of $Cu_2O$ through the N–C/Cu interfacial pathway, mediated by the N–C layer. This process blocks the accumulation of defect-state electrons in $WO_3$, thereby preserving the excited-state electrons in the CB of $Cu_2O$ for prolonged activation (>1 μs). These results corroborate our prior detection of long-lived GSB signals in $Cu_2O$-carbon composites when illuminated under near-infrared irradiation.[50]

Fig. 4b and c show the kinetic curves at 750 nm and the data are fitted using multi-exponential decay components, as listed in Tables S1 and S2. For pristine $WO_3$, a fast ESA decay ($\tau_1 = 36$ ps) was observed, consistent with shallow defect electron trapping at surface defect states. Then, the excited electron was trapped by deep-defect states with a time constant of about 37 ns. In contrast, the kinetic curve of N–C/Cu/$Cu_2O$ was fitted with a multiexponential function with a non-decay offset. The optimal fit reveals two decay components: a fast one with a time constant of 6.0 ps and a slow one of 97 ps. The fast decay process is assigned to the trapping of holes in surface defects, while the 97 ps time constant should reflect the movement of electrons to deep-trapped states (process 1 in Fig. 4d). The 1.1 ns time constant reflects carrier de-trapping, which drives the

formation of GSB (process 2 in Fig. 4d). The GSB recovers within 18 ns and is followed by an ESA signal with a time constant of 48 ns (process 3 in Fig. 4d). Notably, the heterojunction ($WO_3$/N–C/Cu/$Cu_2O$) exhibits accelerated decay processes with the time constants of 2.6 ps and slow 153 ps. The absence of the de-trapping process in $WO_3$/N–C/Cu/$Cu_2O$ suggests interfacial charge transfer from $WO_3$ to $Cu_2O$. Then, the kinetic behavior of the heterojunction demonstrates a dual-phase evolution: GSB recovery (Table S2, $\tau_1 = 3.0$ ns and $\tau_2 = 19$ ns) followed by an ESA ($\tau_3 = 36$ ns) signal, evidencing defect-engineered carrier lifetime extension *via* the N-doped carbon layer. Remarkably, the $WO_3$/N–C/Cu/$Cu_2O$ heterojunction shows unique behavior: following the initial GSB recovery, a secondary bleach feature grows stronger, with carrier lifetimes surpassing 1 μs. This divergence originates from the rapid interfacial recombination of conduction band (CB) electrons in $WO_3$ with valence band (VB) holes in $Cu_2O$ at the heterojunction interface (Fig. 3e), thereby suppressing the charge transfer pathway (process 3) observed in N–C/Cu/$Cu_2O$. Consequently, the CB electrons in $Cu_2O$ remain energetically active, significantly enhancing catalytic performance through interfacial carrier engineering.

To explore the role of the $WO_3$/N–C/Cu/$Cu_2O$ interface in photocatalytic performance, a series of heterojunctions with various W-to-Cu molar ratios have been synthesized. The samples labelled as C/Cu, W/C/Cu-1, W/C/Cu-2. W/C/Cu-3, and W/C/Cu-4 represent the $WO_3$/N–C/Cu/$Cu_2O$ heterojunctions with W-to-Cu molar ratios of 0, 1 : 3, 1 : 2, 2 : 3, and 3 : 4, respectively. As shown in the SEM images in Fig. 5a, as the W-to-Cu molar ratio increases, the density of $WO_3$ particles deposited on the surface of the N–C/Cu/$Cu_2O$ cuboctahedra increases significantly. The homo-coupling reaction of phenylacetylene to 1,4-diphenylbutadiyne has been chosen as the target reaction (Fig. S12). As illustrated in Fig. 5a and b, the deposition of $WO_3$ to form a $WO_3$/N–C/Cu/$Cu_2O$ interface enhances the photocatalytic activity of N–C/Cu/$Cu_2O$. The photocatalytic performance of the $WO_3$/N–C/Cu/$Cu_2O$ heterojunction improves with the addition of $WO_3$ until the W-to-Cu molar ratio reaches 3 : 4. Specifically, the photocatalytic activity of W/C/Cu-4 is lower than that of W/C/Cu-3. This decrease is mainly attributed to the excessive loading of $WO_3$, which obstructs the photoexcitation of $Cu_2O$ and disrupts the smooth operation of the Z-scheme photogenerated carrier migration mechanism. Fig. 5c illustrates the comparative photocatalytic activities of $WO_3$/N–C/Cu/$Cu_2O$ (with a W-to-Cu molar ratio of 2 : 3), N–C/Cu/$Cu_2O$, $WO_3$/$Cu_2O$, $Cu_2O$, and $WO_3$ in the terminal alkyne homo-coupling reaction. The results indicate that the photocatalytic activity follows the order: $WO_3$/N–C/Cu/$Cu_2O$ > N–C/Cu/$Cu_2O$ > $WO_3$/$Cu_2O$ > $Cu_2O$ > $WO_3$. Based on the reaction mechanism of terminal alkyne homo-coupling,[51–56] pristine $WO_3$ cannot generate the crucial Cu(I)-related intermediates and therefore exhibits no catalytic activity for this reaction. The catalytic performance of N–C/Cu/$Cu_2O$ and $WO_3$/$Cu_2O$ heterojunctions surpasses that of pristine $Cu_2O$ due to the directional charge transfer at the heterojunction interface, which facilitates the conversion of Cu(I)-related species into electron-deficient Cu(II)-related species. This conversion enables the dissociation of Cu(II)-related species, leading to the formation of $C_{sp}$–$C_{sp}$ homo-coupling products.[48] Furthermore, the photocatalytic efficiency of the $WO_3$/N–C/Cu/$Cu_2O$ heterojunction is significantly enhanced compared to N–C/Cu/$Cu_2O$ and $WO_3$/$Cu_2O$. It benefits from both the internal charge rearrangement within the Cu(I)-related species and the generation of $\cdot O_2^-$, which further promotes the transformation into Cu(II)-related species. Since there is no obvious relationship between the surface area and the activity (Fig. S13), the significantly enhanced photocatalytic activity of $WO_3$/N–C/Cu/$Cu_2O$ for the terminal alkyne homo-coupling reaction, as compared to $WO_3$/$Cu_2O$, offers compelling evidence supporting the Z-scheme migration mechanism within the $WO_3$/N–C/Cu/$Cu_2O$ heterojunction. In addition, we have conducted experiments to prove the important influences of photo-generated holes and electrons and $\cdot O_2^-$ (Fig. S14). The cycle stability of the catalysts has been evaluated (Fig. 5d), and the $WO_3$/N–C/Cu/$Cu_2O$ heterojunction demonstrates outstanding cycle stability with no obvious loss of photocatalytic efficiency and no changes in the structure and morphology after three cycles of photocatalytic reactions (Fig. S15). To further validate the high catalytic activity of $WO_3$/

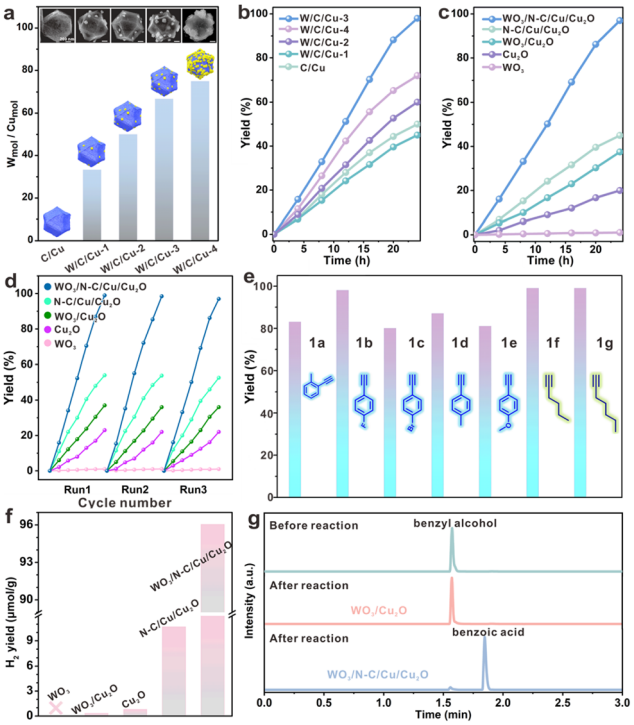


Fig. 5 (a) The histogram of different W/Cu contents and the corresponding SEM images, (b) the yield of homo-coupling of phenylacetylene over different W/Cu content samples, (c) the yield of homo-coupling of phenylacetylene over $WO_3$/N–C/Cu/$Cu_2O$, N–C/Cu/$Cu_2O$, $Cu_2O$, $WO_3$/$Cu_2O$, and $WO_3$ samples, (d) stability test of the various photocatalysts for the homo-coupling of phenylacetylene, (e) performance of $WO_3$/N–C/Cu/$Cu_2O$ in homo-coupling of various alkynes, (f) the photocatalytic hydrogen yields over $WO_3$/N–C/Cu/$Cu_2O$, N–C/Cu/$Cu_2O$, $Cu_2O$, $WO_3$/$Cu_2O$, and $WO_3$ samples with benzyl alcohol as the hole capturer, (g) the retention time of different aqueous solutions (unreacted benzyl alcohol solution and reaction solutions with $WO_3$/$Cu_2O$ and $WO_3$/N–C/Cu/$Cu_2O$ as photocatalysts, respectively) detected by liquid chromatography.

N–C/Cu/$Cu_2O$, we have conducted the photocatalytic oxidation of various alkyne substrates under identical conditions. As shown in Fig. 5e, the yields of the corresponding target products ranged from 80% to 99%, confirming that the Z-scheme $WO_3$/N–C/Cu/$Cu_2O$ heterojunction is an exceptional photocatalyst under blue light ($\lambda = 450$ nm).

To further confirm the Z-scheme mechanism of the $WO_3$/N–C/Cu/$Cu_2O$ heterojunction and its influence on catalytic performance, the $WO_3$/N–C/Cu/$Cu_2O$ heterojunction has been employed as a catalyst for photocatalytic hydrogen production using benzyl alcohol as the hole capture. As illustrated in Fig. 5f, under irradiation of blue light, the hydrogen production efficiency of the five samples follows the order: $WO_3$/N–C/Cu/$Cu_2O$ > N–C/Cu/$Cu_2O$ > $Cu_2O$ > $WO_3$/$Cu_2O$ > $WO_3$. Among them, the CB potential of $WO_3$ is more positive than the $H^+/H_2$ potential (0 V *vs.* NHE); therefore, $WO_3$ lacks the ability to photocatalyze hydrogen production. The hydrogen production rate of $WO_3$/N–C/Cu/$Cu_2O$ is 9 times and 120 times higher than that of N–C/Cu/$Cu_2O$ and $Cu_2O$, respectively, indicating that the constructed $WO_3$/N–C/Cu/$Cu_2O$ heterojunction interface can significantly facilitate efficient migration and separation of photogenerated carriers. Moreover, the hydrogen production of $WO_3$/N–C/Cu/$Cu_2O$ is 300 times greater than that of $WO_3$/$Cu_2O$, suggesting that the photogenerated electrons in $WO_3$/N–C/Cu/$Cu_2O$ are predominantly accumulated in the CB of $Cu_2O$, thereby promoting the reduction reaction for hydrogen production. The reaction solutions after the photocatalysis over these five catalysts have been analyzed using liquid chromatography, and the results are presented in Fig. 5g and S16. With $WO_3$/$Cu_2O$, N–C/Cu/$Cu_2O$, and $Cu_2O$ as photocatalysts, only unreacted benzyl alcohol can be detected, indicating that no conversion of benzyl alcohol to benzoic acid has occurred under these conditions. In contrast, in the reaction solution of $WO_3$/N–C/Cu/$Cu_2O$ and $WO_3$, both benzyl alcohol and benzoic acid have been observed. The benzoic acid can be produced *via* the oxidation of benzyl alcohol by ·OH or photogenerated holes. This observation can be attributed to the VB position of $WO_3$ (+2.62 V *vs.* NHE) being more positive than the redox potential of the benzaldehyde/benzoic acid couple (+2.5 V *vs.* NHE).[49] These findings suggest that in the $WO_3$/N–C/Cu/$Cu_2O$ system, photogenerated holes ultimately accumulate on the VB of $WO_3$ to participate in the oxidation reaction, providing further strong evidence for the preserved high redox potentials in the obtained Z-scheme $WO_3$/N–C/Cu/$Cu_2O$ heterojunction.

To further verify the effective separation and migration of photogenerated carriers within the constructed Z-scheme $WO_3$/N–C/Cu/$Cu_2O$ heterojunction, we have conducted measurements of photocurrent density and electrochemical impedance spectroscopy (EIS) for $WO_3$/N–C/Cu/$Cu_2O$, N–C/Cu/$Cu_2O$, $WO_3$/$Cu_2O$, $Cu_2O$, and $WO_3$ samples. As illustrated in Fig. S17a, the photocurrent densities of $WO_3$/N–C/Cu/$Cu_2O$ are 2, 3, 5, and 5 times higher than those of N–C/Cu/$Cu_2O$, $WO_3$/$Cu_2O$, $Cu_2O$, and $WO_3$, respectively. This suggests that the formation of multiple interfaces does not undermine the positive promoting effect of the $WO_3$/N–C/Cu/$Cu_2O$ heterojunction on the separation of photogenerated carriers. The order of EIS radii of these five samples (Fig. S17b) is $WO_3$/N–C/Cu/$Cu_2O$ < N–C/Cu/$Cu_2O$ < $WO_3$/$Cu_2O$ < $Cu_2O$ < $WO_3$. Generally, a smaller arc radius implies higher charge transfer efficiency. Therefore, $WO_3$/N–C/Cu/$Cu_2O$ exhibits the highest charge transfer efficiency among these five samples. This further confirms that the $WO_3$/N–C/Cu/$Cu_2O$ interface in the Z-scheme heterojunction we constructed is sufficiently robust, providing an efficient and smooth pathway for the migration and separation of photogenerated carriers.

## Conclusions

In this work, a "post-deposition and pyrolysis" synthesis strategy has been employed to fabricate a Z-scheme $WO_3$/N–C/Cu/$Cu_2O$ heterojunction featuring a tightly integrated interface. XPS spectra analysis and work function calculations reveal the opposite directions of interfacial electron migration in $WO_3$/N–C/Cu/$Cu_2O$ and $WO_3$/$Cu_2O$ heterojunctions. These findings preliminarily demonstrate that the modified heterojunction interface can effectively overcome the mismatched work functions of $WO_3$ and $Cu_2O$, control the direction of ground-state electron migration, and thereby modulate the orientation of the built-in electric field at the interface. The results of EPR and photocatalytic tests have confirmed that the $WO_3$/N–C/Cu/$Cu_2O$ heterojunction can preserve the energetic photogenerated holes of $WO_3$ and the photogenerated electrons of $Cu_2O$ for participation in the redox reaction. The fs-TA spectroscopy elucidates the migration pathway of photogenerated carriers in the $WO_3$/N–C/Cu/$Cu_2O$ heterojunction. Specifically, the photogenerated electrons from $WO_3$ recombine with the photogenerated holes of $Cu_2O$ enriched on Cu through the mediation of the N–C layer, which is a typical Z-scheme charge transfer mechanism. This research not only introduces a novel concept in interface engineering for constructing efficient heterojunction photocatalysts but also provides a synthetic strategy for building effective and compact heterojunction interfaces.

## Author contributions

The manuscript was written through contributions from all authors. All authors have given approval to the final version of the manuscript. In detail, H. Gao, X. He, and J. Li contributed equally to the investigation and data curation, C. Qin supported the visualization, S. Zhi supported the data curation, L. Yang and J. Zhao contributed to the software, and L. Sun, W. Zhan, and X. Han contributed to the conceptualization and writing.

## Conflicts of interest

There are no conflicts to declare.

## Data availability

The data supporting this article have been included as part of the supplementary information (SI). Supplementary information: experimental details, characterization data for the reference samples, and the supplementary data for $WO_3$/N-C/Cu/

$Cu_2O$ heterojunctions. See DOI: https://doi.org/10.1039/d5sc05362e.

## Acknowledgements

This work was supported by the Xuzhou Key Research and Development Program (Social Development) (No. KC23298), the National Natural Science Foundation of China (Grant No. 22271122), the Natural Science Foundation of the Jiangsu Higher Education Institutions of China (24KJA150003), and the Basic Research Program of Jiangsu (BK20253049). We thank the Materials Characterization Center of East China Normal University for help with the femtosecond TA measurement.

## Notes and references

1 X. Sun, X. Zhang and Y. Xie, *Matter*, 2020, **2**, 842–861.
2 Z. Zhang, X. Chen, H. Zhang, W. Liu, W. Zhu and Y. Zhu, *Adv. Mater.*, 2020, **32**, 1907746.
3 J.-R. Huang, W.-X. Shi, S.-Y. Xu, H. Luo, J. Zhang, T.-B. Lu and Z.-M. Zhang, *Adv. Mater.*, 2024, **36**, 2306906.
4 Y.-J. Wang, X. Cheng, N.-N. Ma, W.-Y. Cheng, P. Zhang, F. Luo, W.-X. Shi, S. Yao, T.-B. Lu and Z.-M. Zhang, *Angew. Chem., Int. Ed.*, 2025, **64**, e202423204.
5 S. Zhao, S.-S. Shen, L. Han, B.-C. Tian, N. Li, W. Chen and X.-B. Li, *Rare Met.*, 2024, **43**, 4038–4055.
6 R. Chen, S. Pang, H. An, J. Zhu, S. Ye, Y. Gao, F. Fan and C. Li, *Nat. Energy*, 2018, **3**, 655–663.
7 L. Pan, M. Ai, C. Huang, L. Yin, X. Liu, R. Zhang, S. Wang, Z. Jiang, X. Zhang, J.-J. Zou and W. Mi, *Nat. Commun.*, 2020, **11**, 418.
8 Z. Wang, Z. Lin, S. Shen, W. Zhong and S. Cao, *Chin. J. Catal.*, 2021, **42**, 710–730.
9 J. Low, J. Yu, M. Jaroniec, S. Wageh and A. A. Al-Ghamdi, *Adv. Mater.*, 2017, **29**, 1601694.
10 D. Zhao, Y. Wang, C.-L. Dong, Y.-C. Huang, J. Chen, F. Xue, S. Shen and L. Guo, *Nat. Energy*, 2021, **6**, 388–397.
11 X. Chen, J. Wang, Y. Chai, Z. Zhang and Y. Zhu, *Adv. Mater.*, 2021, **33**, 2007479.
12 J. Fu, J. Yu, C. Jiang and B. Cheng, *Adv. Energy Mater.*, 2018, **8**, 1701503.
13 Q. Xu, L. Zhang, J. Yu, S. Wageh, A. A. Al-Ghamdi and M. Jaroniec, *Mater. Today*, 2018, **21**, 1042–1063.
14 P. Zhou, J. Yu and M. Jaroniec, *Adv. Mater.*, 2014, **26**, 4920–4935.
15 Y. Li, K. Chen, X. Wang, Z. Xiao, G. Liao, J. Wang, X. Li, Y. Tang, C. He and L. Li, *Chemosphere*, 2022, **308**, 136259.
16 G. Zhang and Y. Wang, *Polyoxometalates*, 2023, **2**, 9140020.
17 X. Li, Q. Liu, F. Deng, J. Huang, L. Han, C. He, Z. Chen, Y. Luo and Y. Zhu, *Appl. Catal. B Environ. Energy*, 2022, **314**, 121502.
18 M. Zhang, Y. Mao, X. Bao, G. Zhai, D. Xiao, D. Liu, P. Wang, H. Cheng, Y. Liu, Z. Zheng, Y. Dai, Y. Fan, Z. Wang and B. Huang, *Angew. Chem., Int. Ed.*, 2023, **62**, e202302919.
19 H. Zhao, L. Wang, G. Liu, Y. Liu, S. Zhang, L. Wang, X. Zheng, L. Zhou, J. Gao, J. Shi and Y. Jiang, *ACS Catal.*, 2023, **13**, 6619–6629.
20 P. Xia, S. Cao, B. Zhu, M. Liu, M. Shi, J. Yu and Y. Zhang, *Angew. Chem., Int. Ed.*, 2020, **59**, 5218–5225.
21 J. Du, I. Ahmad, I. M. Ashraf, F. B. M. Ahmed, A. Aslam, I. Ali, A. Mohammad and M. A. Khasawneh, *Int. J. Hydrogen Energy*, 2025, **100**, 1361–1384.
22 W. Wang, S. Mei, H. Jiang, L. Wang, H. Tang and Q. Liu, *Chin. J. Catal.*, 2023, **55**, 137–158.
23 Y. Zhang, Z. Jin, D. Liu, Z. Tan, B. B. Mamba, A. T. Kuvarega and J. Gui, *ACS Appl. Nano Mater.*, 2022, **5**, 5448–5458.
24 S. Wu, X. Yu, J. Zhang, Y. Zhang, Y. Zhu and M. Zhu, *Chem. Eng. J.*, 2021, **411**, 128555.
25 X. Li, Y. Wan, F. Deng, Y. Zhou, P. Chen, F. Dong and J. Jiang, *Chin. Chem. Lett.*, 2025, **36**, 111418.
26 L. Zhang, J. Zhang, H. Yu and J. Yu, *Adv. Mater.*, 2022, **34**, 2107668.
27 Q. Xu, L. Zhang, B. Cheng, J. Fan and J. Yu, *Chem*, 2020, **6**, 1543–1559.
28 J. Fu, Q. Xu, J. Low, C. Jiang and J. Yu, *Appl. Catal., B*, 2019, **243**, 556–565.
29 Q. Xu, S. Wageh, A. A. Al-Ghamdi and X. Li, *J. Mater. Sci. Technol.*, 2022, **124**, 171–173.
30 J. Wang, Q. Zhang, F. Deng, X. Luo and D. D. Dionysiou, *Chem. Eng. J.*, 2020, **379**, 122264.
31 P. Shandilya, S. Sambyal, R. Sharma, P. Mandyal and B. Fang, *J. Hazard. Mater.*, 2022, **428**, 128218.
32 H. Gong, Y. Zhang, Y. Cao, M. Luo, Z. Feng, W. Yang, K. Liu, H. Cao and H. Yan, *Appl. Catal., B*, 2018, **237**, 309–317.
33 Q. Wei, Y. Wang, H. Qin, J. Wu, Y. Lu, H. Chi, F. Yang, B. Zhou, H. Yu and J. Liu, *Appl. Catal., B*, 2018, **227**, 132–144.
34 R. Camposeco, S. Castillo, V. Rodriguez-Gonzalez, M. Hinojosa-Reyes, M. I. Medina-Alvares and I. Mejia-Centeno, *J. Photochem. Photobiol., A*, 2018, **353**, 114–121.
35 S. J. Hong, S. Lee, J. S. Jang and J. S. Lee, *Energy Environ. Sci.*, 2011, **4**, 1781–1787.
36 J. Jin, J. Yu, D. Guo, C. Cui and W. Ho, *Small*, 2015, **11**, 5262–5271.
37 T. Fukumura, E. Sambandan and H. Yamashita, *Mater. Res. Bull.*, 2017, **94**, 493–499.
38 S. Chen, Y. Hu, S. Meng and X. Fu, *Appl. Catal. B Environ. Energy*, 2014, **150**, 564–573.
39 L. Zhang, Q. Shen, F. Huang, L. Jiang, J. Liu, J. Sheng, Y. Li and H. Yang, *Appl. Surf. Sci.*, 2023, **608**, 155064.
40 X. Li, B. Kang, F. Dong, Z. Zhang, X. Luo, L. Han, J. Huang, Z. Feng, Z. Chen, J. Xu, B. Peng and Z. L. Wang, *Nano Energy*, 2021, **81**, 105671.
41 C. Kim, K. M. Cho, A. Al-Saggaf, I. Gereige and H.-T. Jung, *ACS Catal.*, 2018, **8**, 4170–4177.
42 H. Long, M. Zhao, T. Ma, Z. Lang, S. Zhang and C. Lei, *Mater. Today Commun.*, 2024, **41**, 110871.
43 J. He, D. W. Shao, L. C. Zheng, L. J. Zheng, D. Q. Feng, J. P. Xu, X. H. Zhang, W. C. Wang, W. H. Wang, F. Lu, H. Dong, Y. H. Cheng, H. Liu and R. K. Zheng, *Appl. Catal., B*, 2017, **203**, 917–926.
44 K. Sun, X. Zhao, Y. Zhang, D. Wu, X. Zhou, F. Xie, Z. Tang and X. Wang, *Mater. Chem. Phys.*, 2020, **251**, 123172.
45 S. S. Y. Chui, S. M. F. Lo, J. P. H. Charmant, A. G. Orpen and I. D. Williams, *Science*, 1999, **283**, 1148–1150.

46 D. Zu, Y. Ying, Q. Wei, P. Xiong, M. S. Ahmed, Z. Lin, M. M.-J. Li, M. Li, Z. Xu, G. Chen, L. Bai, S. She, Y. H. Tsang and H. Huang, *Angew. Chem., Int. Ed.*, 2024, **63**, e202405756.
47 X. Ruan, D. Meng, C. Huang, M. Xu, D. Jiao, H. Cheng, Y. Cui, Z. Li, K. Ba, T. Xie, L. Zhang, W. Zhang, J. Leng, S. Jin, S. K. Ravi, Z. Jiang, W. Zheng, X. Cui and J. Yu, *Adv. Mater.*, 2024, **36**, 2309199.
48 S. Cao, B. Shen, T. Tong, J. Fu and J. Yu, *Adv. Funct. Mater.*, 2018, **28**, 1800136.
49 F. M. Pesci, A. J. Cowan, B. D. Alexander, J. R. Durrant and D. R. Klug, *J. Phys. Chem. Lett.*, 2011, **2**, 1900–1903.
50 X. Han, X. He, L. Sun, X. Han, W. Zhan, J. Xu, X. Wang and J. Chen, *ACS Catal.*, 2018, **8**, 3348–3356.
51 S. E. Allen, R. R. Walvoord, R. Padilla-Salinas and M. C. Kozlowski, *Chem. Rev.*, 2013, **113**, 6234–6458.
52 Z.-H. Zhang, X.-Y. Dong, X.-Y. Du, Q.-S. Gu, Z.-L. Li and X.-Y. Liu, *Nat. Commun.*, 2019, **10**, 5689.
53 X.-Y. Dong, J.-T. Cheng, Y.-F. Zhang, Z.-L. Li, T.-Y. Zhan, J.-J. Chen, F.-L. Wang, N.-Y. Yang, L. Ye, Q.-S. Gu and X.-Y. Liu, *J. Am. Chem. Soc.*, 2020, **142**, 9501–9509.
54 K. Kamata, S. Yamaguchi, M. Kotani, K. Yamaguchi and N. Mizuno, *Angew. Chem., Int. Ed.*, 2008, **47**, 2407–2410.
55 Y. Zhu and Y. Shi, *Org. Biomol. Chem.*, 2013, **11**, 7451–7454.
56 W. Lu, X. Yu and M. Bao, *Green Chem.*, 2023, **25**, 5123–5127.
57 X. Yan, T. Xu, W. Zhan, Y. Yang, Y. Yu, J. Yi, X. He, L. Yang, J. Zhao, L. Sun and X. Han, *Nano Res.*, 2024, **17**, 6895–6902.
58 H. G. Roth, N. A. Romero and D. A. Nicewicz, *Synlett*, 2016, **27**, 714–723.